



Capability to detect and localize typical defects of laser powder bed fusion (L-PBF) process: an experimental investigation with different non-destructive techniques

Ester D'Accardi¹ · Rainer Krankenhagen² · Alexander Ulbricht² · Matthias Pelkner² · Rainer Pohl² · Davide Palumbo¹ · Umberto Galietti¹

Received: 6 October 2021 / Accepted: 27 March 2022 / Published online: 19 April 2022
© The Author(s) 2022, corrected publication 2022

Abstract

Additive manufacturing (AM) technologies, generally called 3D printing, are widely used because their use provides a high added value in manufacturing complex-shaped components and objects. Defects may occur within the components at different time of manufacturing, and in this regard, non-destructive techniques (NDT) represent a key tool for the quality control of AM components in many industrial fields, such as aerospace, oil and gas, and power industries. In this work, the capability of active thermography and eddy current techniques to detect real imposed defects that are representative of the laser powder bed fusion process has been investigated. A 3D complex shape of defects was revealed by a μ CT investigation used as reference results for the other NDT methods. The study was focused on two different types of defects: porosities generated in keyhole mode as well as in lack of fusion mode. Different thermographic and eddy current measurements were carried out on AM samples, providing the capability to detect volumetric irregularly shaped defects using non-destructive methods.

Keywords Typical defects in metal additive manufacturing (AM) · Non-destructive techniques NDT · Thermographic testing (TT) · Eddy current testing (ET) · Micro-computed tomography (μ CT) · Laser powder bed fusion (L-PBF) process · Keyhole and lack of fusion defects

1 Introduction

Additive manufacturing (AM) represents a series of manufacturing and technologies processes in which components are built by depositing materials layer by layer. These techniques are increasingly taking a relevant place in the manufacturing industry, to produce different materials in different fields. So far, parts in plastic, metal and ceramics have been successfully manufactured by additive techniques [1].

Regarding metals, among the powder bed fusion (PBF) technologies, laser powder bed fusion process (L-PBF) [1], also known as selective laser melting (SLM), allows the manufacture of components suitable for high demanding

applications in mechanical, aerospace, medical, and motor racing fields. Generally, L-PBF is an additive manufacturing process that uses a laser to melt portions of powder in thin layers of material to build up the desired shape, changing different parameters and printing conditions. Once the layer is solidified, a new powder layer is spread, and the process repeats until the part is created [2].

Different input process parameters, such as laser power, laser scanning speed, powder flow rate and scanning strategy, profoundly affect L-PBF processes and the quality of the final product. It is usual to distinguish process parameters into either controllable or so possible to modify from the operator, such as laser power and scanning speed, or predefined (set at the beginning of each process) material properties, such as powder size, thermophysical properties and distribution [1].

Any unexpected variation of the process parameters, as demonstrated in different previous works [2–13], can produce defects like pores, high surface roughness and thermal cracking.

✉ Ester D'Accardi
ester.daccardi@poliba.it

¹ Dipartimento di Meccanica, Matematica e Management, Politecnico Di Bari, Via Orabona 4, 70125 Bari, Italy

² Bundesanstalt für Materialforschung und -prüfung (BAM), Unter den Eichen 87, 12205 Berlin, Germany

Pores, that represent the typical and widespread defects in AM, can be generated by different mechanisms. First, pores can be generated in keyhole mode when some AM processes parameters involve very high-power density, with an increase of laser scanning speed. Without careful control of keyhole mode melting, these pores can become unstable, larger and uncontrollable, causing voids inside the material. Second, lack of fusion porosity can be caused by inadequate molten pool penetration of an upper layer into the previously deposited one [2–13]. In this case, diffuse porosities can be produced due to the reduction of laser power. Finally, it is possible to find gaps when the laser inadvertently turns off during the print of the component.

The inspection and thermophysical characterization of powder metal parts at different points during the manufacturing process, online and offline, play a crucial role for several decades, with great attention on the correct use of non-destructive testing (NDT), or to their combination and simultaneous use. For advanced manufacturing, there are potential benefits of online monitoring by means of NDT techniques, as demonstrated in some recent works that involve the use of passive thermography (TT) and spectroscopy [14–16]. This can potentially lead to significant production benefits resulting from the savings of time, material, and processing expenses. On the other side, most quality engineers have focused their attention on the final part inspection, in offline controls, with the aim to improve and automatize the quality inspection of the final component.

Typical NDT methods can involve surface, subsurface and volumetric inspections. In the case of surface inspection, visual tests are widely used generally using a $10\times$ visual enhancement or penetrant tests (by means of fluorescent liquid for increase the sensitivity) [17]. Instead, among the volumetric methods, X-ray, especially digital radiography (DR), computed tomography (CT) and micro-computed tomography (μ CT) currently provide the most reliable inspections and reference results in AM [5]. However, these techniques are time-consuming and require expensive equipment making them not suitable for extensive controls for industrial applications.

Other techniques include the use of acoustic and ultrasonic measurements, especially for the investigations of microstructure and mechanical properties. However, their use requires surface polishing to ensure full contact, and sometimes they are semi-non-destructive [18–20].

Contact and non-contact profilometry, for geometric accuracy and surface roughness characterization, is widespread and easy to use, although limited to external, accessible surfaces only [21].

In the last years, passive and active thermography techniques have been used for monitoring the AM process or for the non-destructive testing of AM components [20, 22–25]. Thermography offers the advantages of being relatively

rapid and non-contact technique, as compared to already mentioned scanning techniques, like ultrasonic, and adaptable to various temperature-inducing methods, as, for example, laser, hot air, halogen and flash lamp, ultrasonic, hot water, eddy current, etc., which allows the technique to be applied to parts difficult to access. Besides, thermography has the additional advantage, pertinent and attractive to additive manufacturing, of being less sensitive to surface roughness compared to other types of non-destructive testing that require a direct contact with the sample such as ultrasound, for example. When applied to metals, the choice of excitation source and thermal camera (the use of a high-speed one is often mandatory) depends on the type of defects that are of interest, and, obviously on their size (depth, diameter, and shape).

On the other hand, eddy current testing (ET) is often used to identify cracking and corrosion in conductive components' surfaces [26–29]. Its utility comes from the possibility to investigate various depths changing the frequency of the probe [30]. Nevertheless, the standard penetration depth of the magnetic field is limited due to conductivity and permeability besides frequency and only regions near the surface can be investigated using this testing method [26]. Few references were found to the use of TT [22–25] and ET [31, 32] as offline controls in the additive manufacturing literature and, more in general, very few works focus on the quantitative comparison among the obtained results in terms of defect detection for AM parts using different NDT methods [23].

The aim of this work is to identify and characterize induced defects produced by the AM process for investigating the capability of NDT methods in detecting volumetric, complex, and real shape defects representative for regions manufactured with keyhole mode, as well as regions with a lack of fusion. Two samples made of AISI 316L steel, produced using L-PBF process, were investigated with μ CT as reference method. Then, two other NDT techniques, commonly used for detecting superficial and sub-superficial defects, have been used for characterizing the induced defects: the thermographic testing (TT) and the eddy current testing (ET). Finally, the capability of TT and ET techniques in detecting the imposed defects has been investigating by comparison with the well-established μ CT technique.

Since three different non-destructive techniques have been used in this work, the results of each technique will be presented in a different section, reporting separately the experimental set-up and data analysis, while the discussion of strong and weak points of each technique is reported in the final section.

2 Materials and methods

2.1 Inspected material, process parameters and defects geometry

The two analyzed samples are part of a collection of different samples made of AISI 316L, produced by means of the L-PBF technique, changing the process parameters and the defects shape in different regions of the specimens. Figure 1a shows the surface of the investigated specimens that is as the surface appears after the AM process, without post-treatments. The laser power of 275 W and the scanning speed of 700 mm/s were the main process parameters used to print these specimens. The cuboid geometry was built up with an alternating meander stripe scanning pattern, where the orientation was rotated by 90° from layer to layer, considering also more details that can be found in [14]. For the sample indicated as PK007 (Fig. 1a), buried regions were produced increasing the energy input by reducing the scanning speed down to 300 mm/s (275 W; 300 mm/s). Instead, for the sample PK010 (Fig. 1b), lack of fusion diffused porosity was induced within the same regions, same intended shape and positions reducing the energy density by decreasing the laser power during the process (150 W; 700 mm/s). In this way, in both cases, a deviation from the optimum process parameters has been obtained in four predefined regions of the specimen, and for specific layers of the material. No further heat treatment was performed to preserve the induced defects or to improve the quality of the final surface. The specimens were cut in different parts (4 parts for PK007 and 2 parts for PK010) to perform the μ CT investigation (Fig. 1).

The intended shapes and 3D dimensions of the induced defects are depicted in Fig. 2 and reported in Table 1, together with the related process parameters.

2.2 Computed tomography set-up and experimental test parameters

The specimens were investigated by micro-computed tomography (μ CT) to assess the shape and size of the internal structures non-destructively. A custom-made μ CT scanner equipped with a Nikon X-ray tube XT 225 with rotating target (Nikon Metrology NV, Leuven, Belgium) and a 4 k flat panel detector (Perkin Ellmer, Santa Clara, USA) was used to scan the specimens. The energy settings were a voltage of $V=201$ kV and a current of $A=550$ μ A. A 0.75 mm thick silver plate was used to harden the beam. To improve the signal-to-noise ratio, the detector was binned to 2 k, and the acquisition time of 2 s was averaged 6 times for all of the 1500 projections. The achieved voxel size was $(30.8 \mu\text{m})^3$. This enables the quantitative analysis of voids larger than $(60 \mu\text{m})^3$. For data analysis, the commercial software VG Studio MAX 3.3 (Volume Graphics GmbH, Heidelberg, Germany) was used. A threshold of 8 voxels was set as a lower threshold for the void analysis (Fig. 3).

2.3 Thermographic set-up and experimental test parameters

The used thermographic set-up is shown in Fig. 4. The tests were carried out in reflection mode, with the heating source and the IR camera placed in front of the sample, on the same side (1—Fig. 4). A diode laser system LDM (500-20 by Laserline GmbH), with a wavelength of 942 nm, was used to stimulate the samples at one surface, with a pattern surface of $39 \times 39 \text{ mm}^2$ (2—Fig. 4). The focal distance between sample and laser optics is 60 cm, that is the optimum for this instrumentation to reach a homogeneous heating (sample size $35 \times 35 \text{ mm}^2 < \text{laser spot size}$).

Different experimental tests for both samples were performed changing the laser pulse duration and the laser

Fig. 1 Surface of the specimens used in this work; **a** PK007 (it is possible to see the division into four parts used for the μ CT measurements and also for ET—in the latter case it is not a requirement required by the instrumentation); **b** PK010

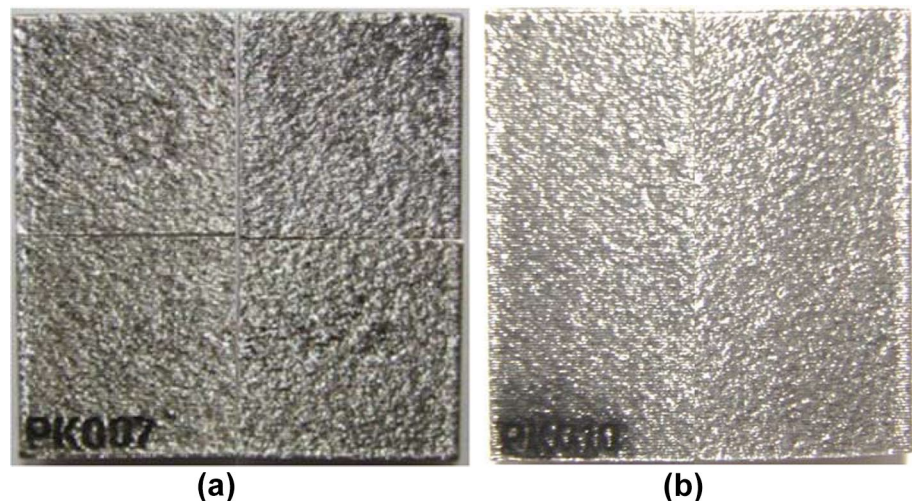


Fig. 2 A simple sketch of the investigated samples and geometry of the intended defects. Process parameters were modified within the indicated regions with a different color to induce the presence of the defects. The nominal 2D dimensions are shown on the right

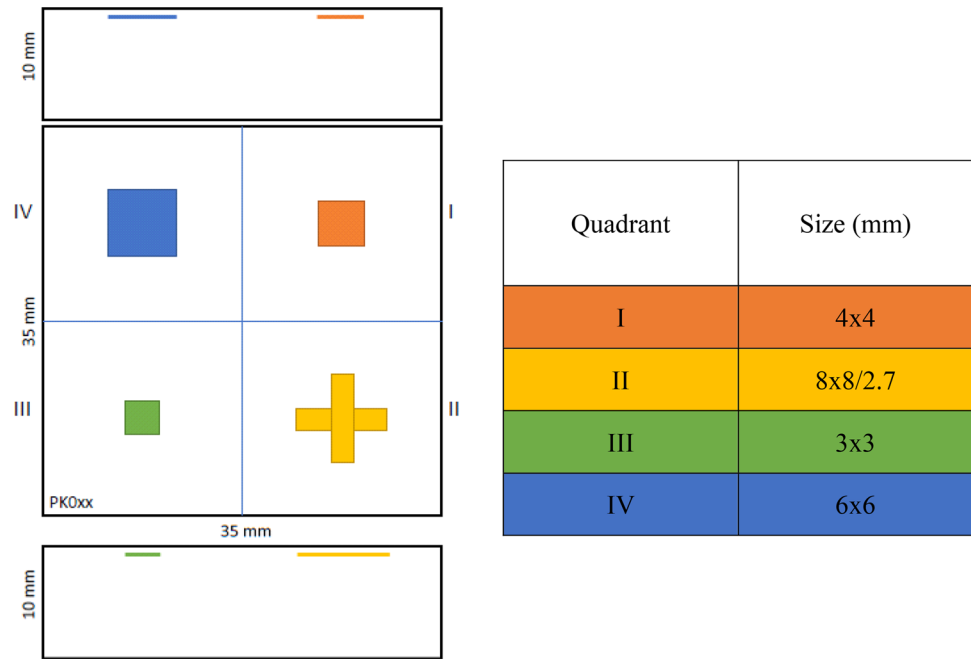


Table 1 Nominal process parameters and some dimensions of the inspected specimens

Sample name	Defect depth (mm)	Defect height (mm)	Size (mm)	Hatch distance (mm)	Energy input (types of induced typical defects)	Scanning laser speed (mm/s)	Scanning laser power (W)
PK007	0.4	1 (20 layers)	Different (Fig. 2)	0.12	High (keyhole)	300	275 (st.)
PK010	0.4	1 (20 layers)	Different (Fig. 2)	0.12	Low (lack of fusion)	700 (st.)	175

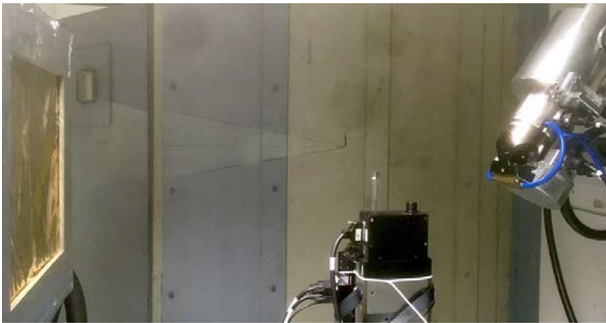


Fig. 3 μ CT set-up for PK007

power with the aim to find, experimentally, the optimum test conditions. In fact, the energy density provided to stimulate the sample depends on the laser power and pulse duration (rectangular pulse), once its shape has been defined. Moreover, the effective adsorbed energy is different from the previous one and it depends on the sample surface conditions. Various considerations in this regard are reported in D'Accardi et al. [22], with some relevant



Fig. 4 Thermographic set-up: specimen (1), excitation source widened laser beam, optic for $39 \times 39 \text{ mm}^2$ (2), Thermal Imaging Camera Infratec ImageIR 8300 hp (3)

indications reported also here as summary in Table 2, with the indication of the absorptivity and the achieved energy density. The final set-up specifications, from an energy point of view, are reported also in the same Table 2 and were the same in both cases for both samples.

The Infratec ImageIR 8300 IR camera (3—Fig. 4) was used to acquire the thermographic tests, with a cooled detector sensitive to the middle infrared wave range (MWIR 3–5 μm), NETD < 25 mK (30 $^{\circ}\text{C}$) in full frame

Table 2 Main experimental set-up parameters and some evaluations in terms of absorptivity and energy density

Input laser power	Laser pulse duration (ms)	Absorptivity at 942 nm	Achieved energy density (Ws/cm ²)	Integration time (μs)	Geometrical resolution (mm/pixel)	Frame rate (Hz)	Acquisition duration (s)
535	980	64%	22.00	486	0.15	500	10

640 × 512 pixels, with acquisition parameters reported in Table 2.

2.4 Eddy current set-up and experimental test parameters

The conventional eddy current instrument ELOTEST B1 V4 [Rohmann GmbH, Frankenthal (Germany)] has been used for the ET investigation. The AC excitation current (max. 100%) was 200 mA effectively. To determine the most reliable results, a set of seven probes with five different frequencies was tested. The best testing results were obtained with the probe AN 16, a BAM development based on two coils wound around two cylindric ferrite cores (diameter 1.6 mm) in an absolute arrangement. This probe comprises a high spatial resolution together with a high penetration depth. The latter is influenced by the electrical conductivity of the specimens which is about 1.3 MS/m for the additively manufactured parts. The standard depths of penetration δ are 1.1 mm for a frequency of 200 kHz and 0.7 mm for a frequency of 500 kHz, which means that the strength of the exciting magnetic field is decreased down to 37% of the exciting magnetic field value at the surface at this depth. Hidden defects can be found in regions deeper than the standard penetration depths [33]; however, the size and geometry of defects and the applied sensing system limit the detectability of deep lying defects. The defects' depth and size of the investigated specimens (see Table 1) are within the possible testing region. However, probe AN 16 has a directional dependence due to its configuration of coils and cores inside the probe. To overcome this behavior, an

absolute probe, A 05, having a core diameter of 0.5 mm has been used. This probe has a unidirectional behavior; however, the sensitivity is reduced leading to a decreased SNR.

The specimens were fixed between four plates of steel under an x - y planar manipulator (see Fig. 5). To protect the probes and the surface of the specimens, a plastic sheet (0.1 mm thick) was placed on top of the specimens and plates. The probes were moved in contact with the plastic sheet.

The spatial resolution for both directions was 0.087 mm and then, a test area of 22 × 22 mm² took about 10 min and an area of 42 × 42 mm took about 24 min.

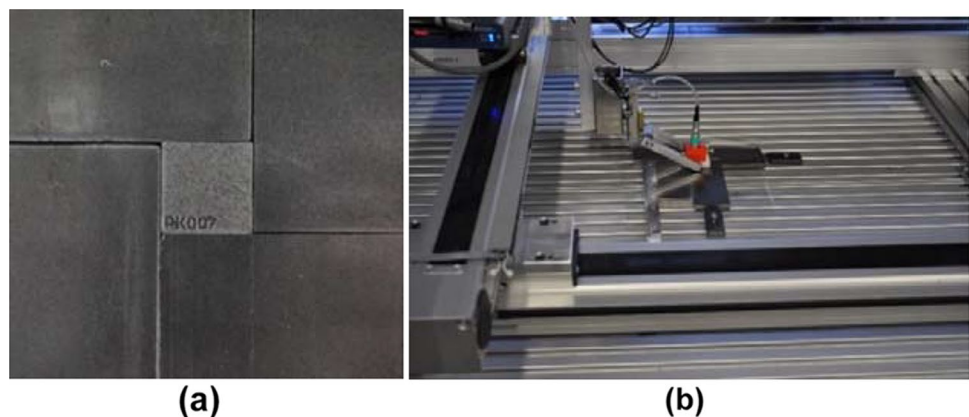
3 Results

3.1 CT results

The PK007 specimen was cut into four pieces to reduce the path length for the μ CT acquisition, and then, increase the signal-to-noise ratio. Figure 6a, b show the results of the 3D reconstructed data for all quarters of PK007. In contrast, Fig. 6c presents a cross-sectional view of the lower right quarter piece along the line in Fig. 6b, while the blue lines indicate the nominal geometry of defects, that are the region with varied deposition parameters.

The colored volume scale corresponds to the pore volume of separated voids, i.e., each color represents a typical pore size, here mainly in the range between 0.2 and 0.8 mm. As depicted in Fig. 6, the porosity in the overexposed sections is not evenly distributed and in some regions appears as large

Fig. 5 (a) Photographs of the test sample fixed between plates, and (b) the used manipulator set-up



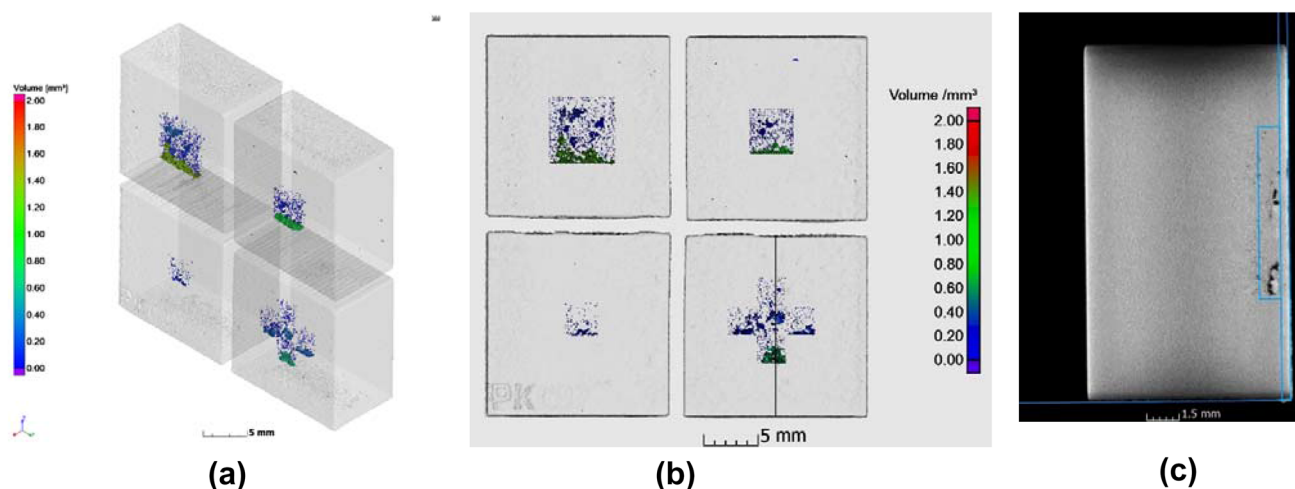


Fig. 6 CT results obtained at PK007 (a) 3D rendering of segmented pores (b), 3D rendering of the projection of all pores (c) virtual cut at the raw data set of the lower right quarter along the black line in (b)

Table 3 PK007 porosity analysis of the 4 sections, related to the volume of the CAD data geometries

Section	Large square	Medium square	Small square	Cross
Porosity	7.5%	6.7%	2.1%	5.6%

connected voids. Except for the small square, some clustering of voids was observed at the center of the induced defect areas. As it can be seen in Fig. 6b, the projection of all voids into the z - y plane seems to form the intended nominal shape of the induced defect areas. The view on the cross-sectional in Fig. 6c reveals the complex shape of pores in the z - x plane and a not constant in-depth position with respect to the imposed defects depth. Please note that the original sample thickness of 3 mm was slightly reduced by removing the final sample from the base plate.

Using the CT data (3D rendering), the following values of porosity were obtained for each region (large square, medium square, small square). It is clear that this value does not include those pores outside the original addressed imposed defects regions (Table 3).

These values are really high in comparison to other reports [34], but not unusual [35]. It can be concluded, that the manufactured specimen includes clearly defective areas as intended.

Figure 7 provides a more detailed view on the morphology of the defect II, which will be used later as a reference defect for comparing the different NDT methods (see Sect. 4).

Further analysis of the PK007 microstructure was reported in D'Accardi et al. [22].

PK010 was only cut into two pieces. The scheme of the presentation the CT results is the same as in Fig. 6. As

depicted in Fig. 8, the shape and spatial distribution of the segmented voids differ significantly from PK007 although the geometric dimensions of the low-exposed respective regions were the same. In the PK010 sample, mainly the left and bottom border of the imposed regions seem to form larger connected voids, while the remaining part of the regions is characterized by diffuse distributed and not connected pores. This effect at the margins is due a poor positioning accuracy within the preprocessing software for the manufacturing process which is obviously not well suited to handle these specific processes with varying parameters. Therefore, the cross-sectional view also shows a short line-shaped cluster region located at the lower section edge (partially covered by the blue line) and few wide-spread single pores.

The estimated porosities for all regions are listed in Table 4.

As demonstrated previously, the work [6] showed the strong influence of laser power on the obtained porosity for AISI 316 steel and reported really high porosity values at lower energies due to lack of fusion. However, a direct comparison is not possible because in Ref. [8] a pulsed laser was applied and the authors provided spatial porosity instead of volume related values. In this work, in the case of the PK010, the obtained porosity is mainly concentrated at the edge regions, thus the real volume porosity (without margin) is much lower. However, the obtained specific edge geometry provides another type of defects as original intended which is perhaps also significant for quality assessments.

As in the case of the PK007 sample, only one quarter was selected for the comparison of the NDT methods: the region indicated as defect IV. Figure 9 contains a more detailed view of the segmented data within this specimen part.

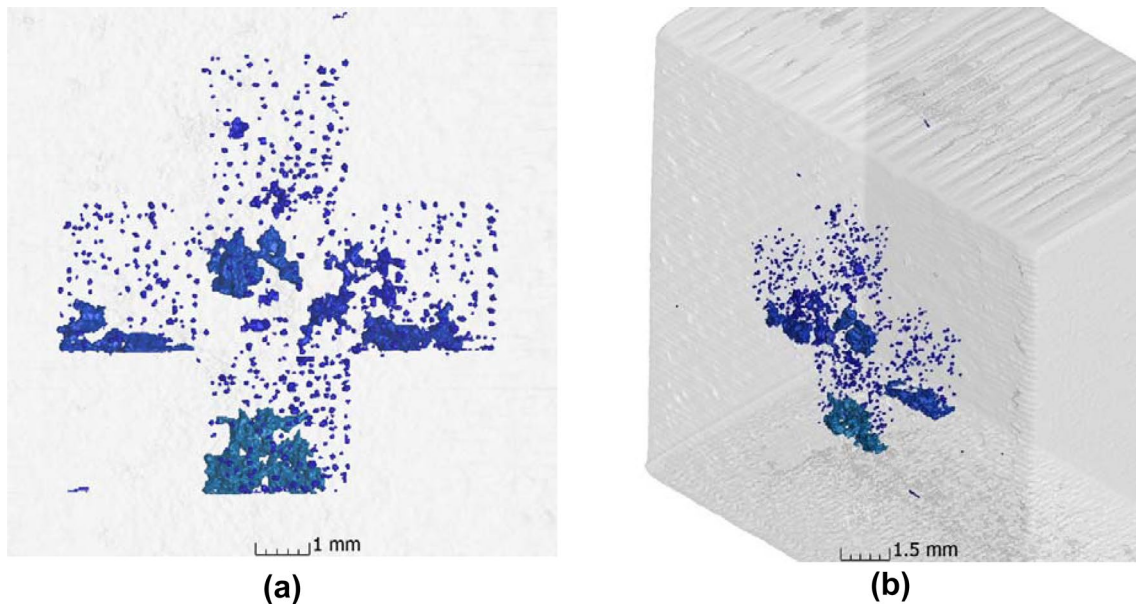


Fig. 7 CT results obtained at the lower right corner of PK007, color scale represent the respective pore size (a) defect II in front view as projection of all segmented pores (b), defect II in 3D view as projection of all segmented pores

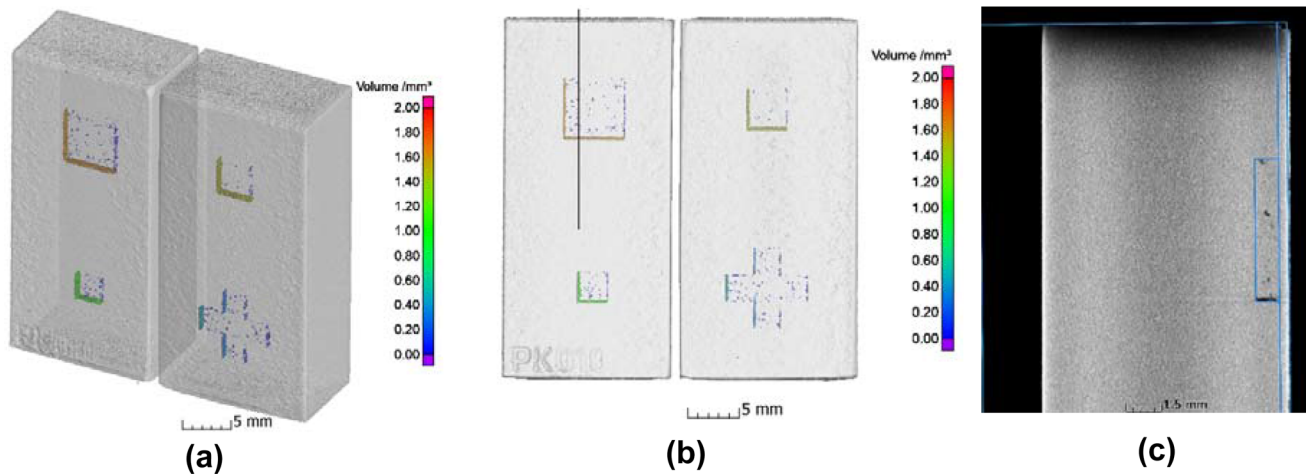


Fig. 8 CT results obtained at PK010 (a) 3D rendering of segmented pores (b), 3D rendering of the projection of all pores (c) virtual cut at the raw data set of the upper left quarter 1 mm along the black line in (b)

Table 4 PK010 Porosity analysis of the four sections related to the volumes of the CAD data geometries

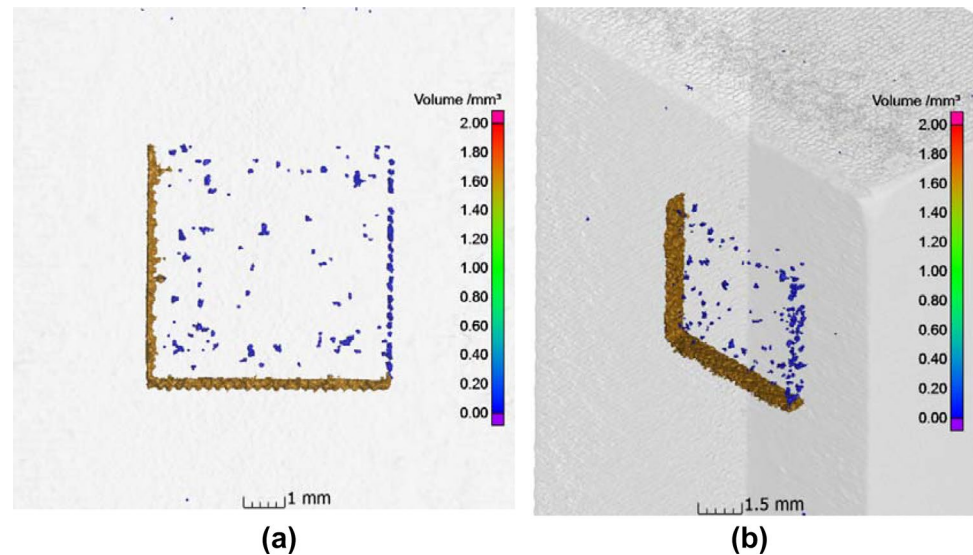
Section	Large square	Medium square	Small square	Cross
Porosity	4.6%	8.4%	10.8%	3.6%

3.2 Thermographic results (TT)

3.2.1 Thermal contrast consideration

As it is known, the thermographic inspection is usually based on the detection of thermal contrasts arising during and after a heating or cooling process. If the state of the surface is homogeneous and then presents a uniform emissivity, thermal contrasts, that can be measured and detecting during the analysis, after homogeneous heating, are related to inside anomalies, defects or structural features.

Fig. 9 CT results obtained at the upper left corner of PK010, color scale represent the respective pore size (a) defect IV in front view as projection of all segmented pores (b), defect IV in 3D view as projection of all segmented pores



Unfortunately, the investigated samples have a non-uniform surface, as characteristic feature of the AM process (as it can be seen in Fig. 1) and this must be taken into account for thermographic characterizations.

In Fig. 10a is shown a “cold” thermogram of the PK007 sample acquired immediately before the heating excitation. The observed or apparent inhomogeneous temperature distribution is caused by spatial variations related to the surface emissivity, that influences strongly the transient behavior of thermal contrasts as shown in Fig. 10b. The apparent maximum temperature increase after a heating pulse differs by almost factor 2 between two different regions of the surface, as more deeply described by D’Accardi et al. [22].

Since defect detection is based on the detection of a measurable thermal contrast, the presence of a non-uniform

emissivity affects the appearing thermal contrasts and then the capability of the technique for detecting internal defects. As already said, the main reason for this behavior is the typical topology of the surface of samples (Fig. 1a), manufactured by the L-PBF process. To overcome the problems derived by a non-uniform emissivity of the sample surface, a post-processing of the raw thermal data is necessary.

3.2.2 Pulsed-phase thermographic results

The pulsed phase thermography (PPT) has been applied as a post-processing algorithm, after the subtraction of the first cold frame, to obtain the classical delta temperature, pixel by pixel. This algorithm is based on a Fourier transformation of the temperature transient measured for each pixel, and

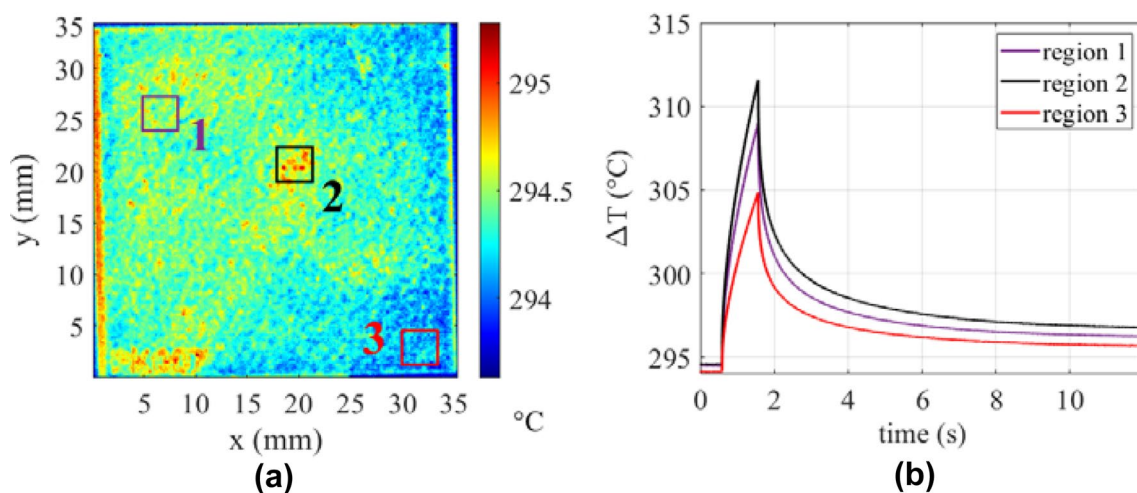


Fig. 10 (a) A thermogram recorded immediately before the heating period and (b) related transients considering three different regions to explain the effects of this strong emissivity variation at the surface

returns, after some well-known mathematical operations, a sequence of $N/2-1$ phase and amplitude images, with N that indicates the total number of frames of the initial sequence, each of which corresponds to a certain frequency of analysis [22, 36–39].

Here, the acquired data are then analyzed in the frequency domain by means of PPT, considering the largest possible multiple of $2N$ based on the duration of the entire sequence (i.e., 4096 frames). A variation of the original approach [36–39] concerns the analysis of a certain part of the entire transient. In this regard, a few of the first thermograms recorded after the heating period were excluded with the aim to discriminate the hot spot pattern caused by the rough surface. Figure 11 shows the different results (same frequency 0.37 Hz), but starting the analysis at a given frame after the heating period, and, in particular, (a) laser switch-on, (b) laser switch-off and (c) 50 ms after the laser is switched off.

In fact, in cases (a) and (b), the phase images contain a series of small hotspots (surface grains) disturbing the detection of inner defects. Contrary, in the case (c), these “hot spots” disappeared allowing a focused view on the

defect-related thermal contrasts. In addition, after the PPT analysis, the entire sequence was filtered with a Gaussian filter ($\text{std}=0.85$), to further reduce the noise. Comparing the results of Fig. 11, the influence of the initial frame considered for the data processing can clearly be recognized.

The following data are related to the phase maps obtained by the PPT algorithm, starting 50 ms after the pulse (that is the case shown firstly as an example in Fig. 11c). Figure 12 shows the results related to the specimen PK007. In particular, the phase maps obtained at three different frequencies were selected. As can be seen from Fig. 12, the quality of results seems to be affected by the frequency at which the phase is considered. The clusters related to defects I, II, and IV show a good contrast at the different frequencies, except for the defect III (left lower quarter). An indication of the presence of this defect emerges only at high frequencies (Fig. 12c).

The same data processing procedure has been carried out for the specimen PK010. The influence of the surface hotspots is not as pronounced as in the case of the PK007

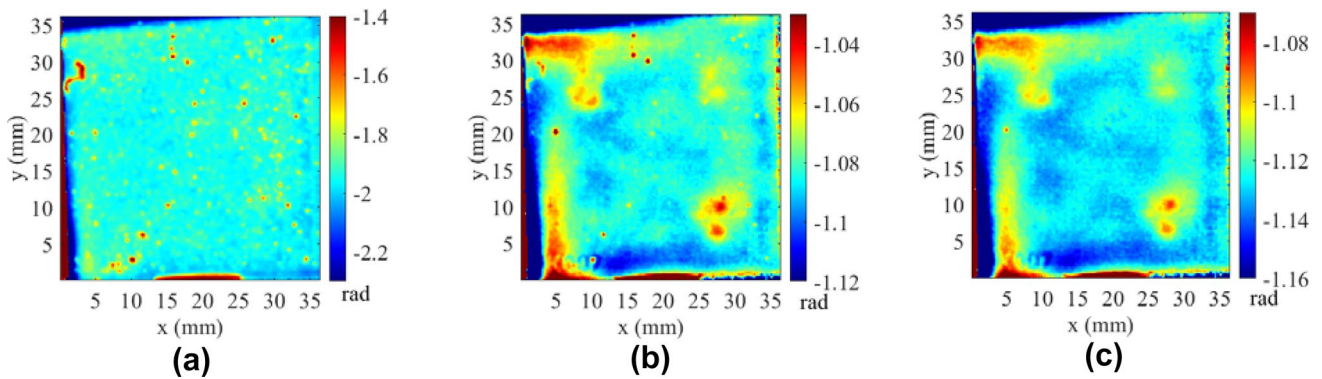


Fig. 11 PPT analysis with different approaches, phase maps related to the frequency of 0.37 Hz (a) heating + cooling, (b) cooling starting from the first frame, (c) cooling starting 50 ms after switching off the laser

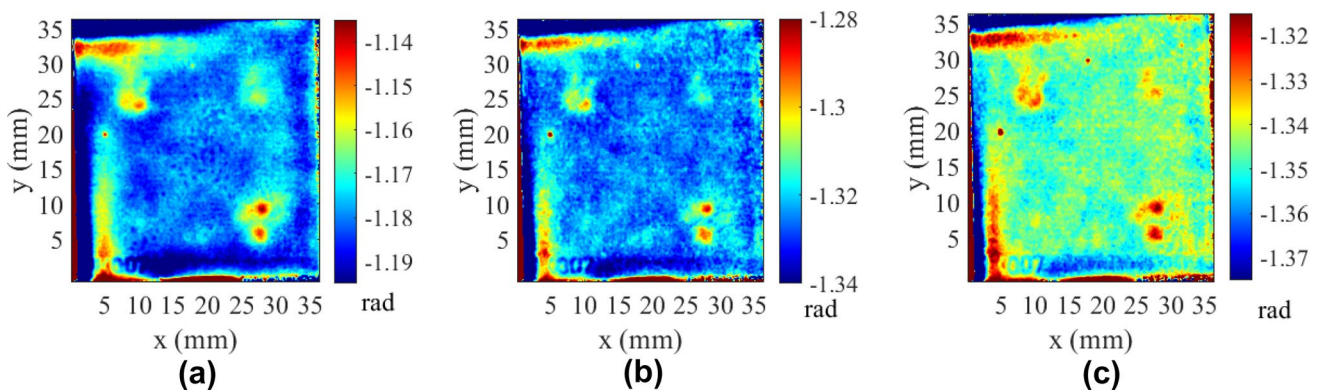


Fig. 12 PK007, PPT algorithm truncation window size 8.192 s, 4096 frames (cooling down, long pulse analysis); maps at 0.48 Hz (a), 1.22 Hz (b) and 1.46 Hz (c)

specimen, but for consistency, we choose again to start the analysis 50 ms after the laser has been switched off.

Upper defects provide clear indications, while the defect in the lower left quadrant (small square) appears in connection with another region of unknown origin near the corner. On the other hand, the cross-shaped defect does not return a clear signal. Furthermore, an edge effect is evident at the bottom right with a strong contrast signal that covers any other signal (Fig. 13).

Comparing the phase results related to PK007 and PK010 samples, it is possible to see how the considered types of defects produce two different thermal signatures in terms of phase signals.

Looking at the obtained TT results, it seems that the technique can detect the considered defects, but the quality of the results is affected by noise phase values due to the intrinsic

surface structure of the material. Moreover, as shown in Fig. 14, the edges of the sample are affected by significant phase variations. The reason for these variations could be due to two different phenomena. The first one is the common “edge effect” that affects all the thermographic results and is due to the heat exchanged by convection and radiation at the boundary surfaces of the sample. In this regard, in Fig. 15 are reported, for both the samples, two regular difference thermograms/frames taken at the end of the heating period (laser off) in which the “edge effect” causes lower temperatures at the specimen boundary.

The second phenomenon could be due to the manufacturing process leading to slightly different microstructures and then to thermal diffusivity variations located on some boundaries of the samples and for which the PPT results

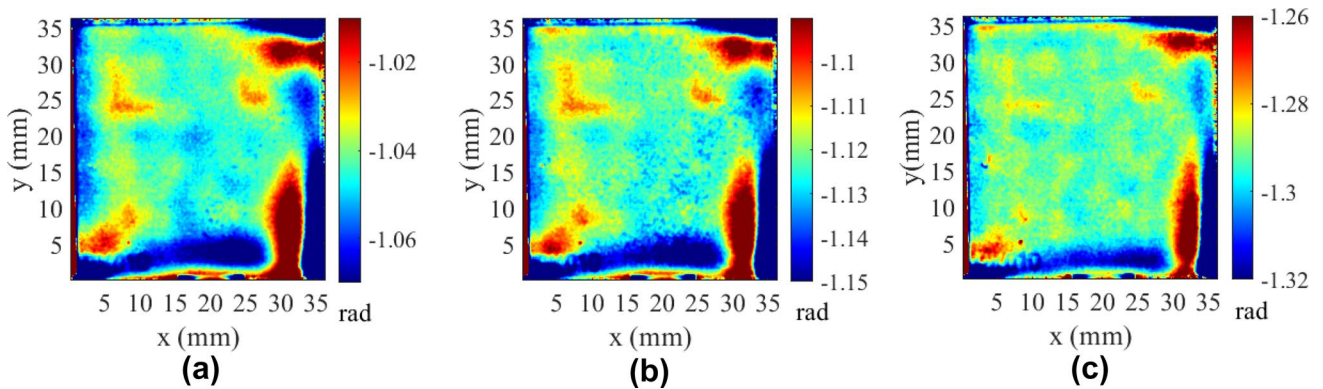


Fig. 13 PK010, PPT algorithm truncation window size 8.192 s, 4096 frames (cooling down, long pulse analysis); maps at 0.24 Hz (a), 0.37 Hz (b) and 0.96 Hz (c)

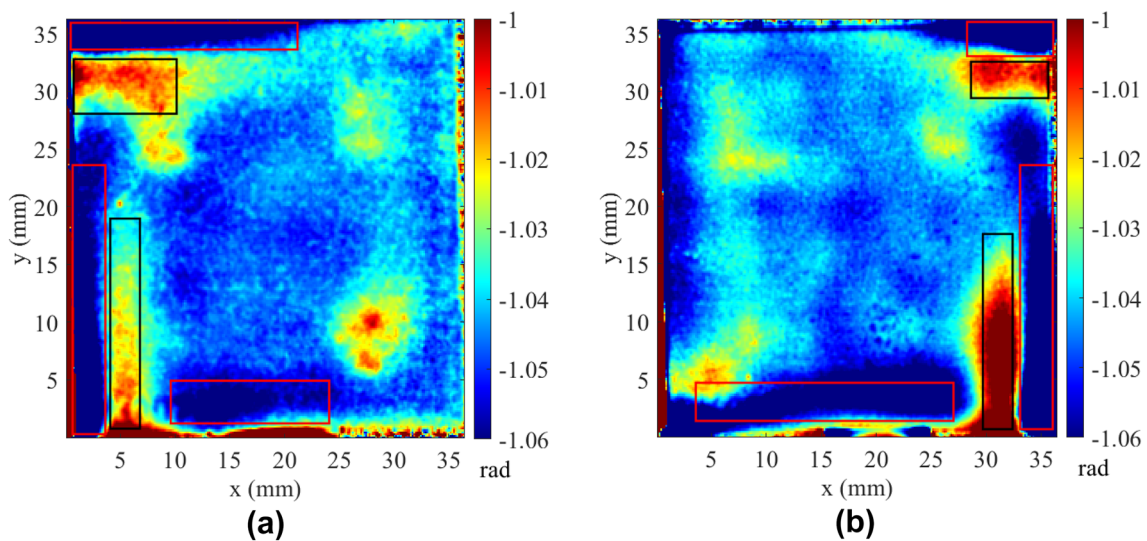


Fig. 14 Striking signatures in parallel orientation to sample edges (indicated by colored rectangles) observed in phase maps (at 0.24 Hz) on both samples: (a) PK007 and (b) PK010

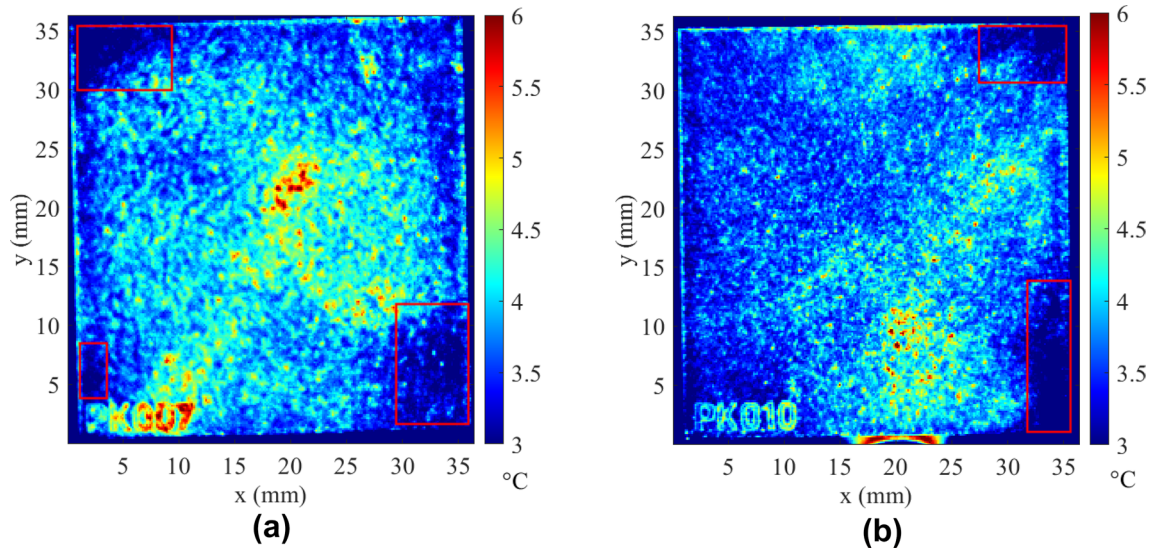


Fig. 15 Different thermograms recorded at the end of the heating period with larger cooler parts at sample edges of both samples: (a) PK007, (b) PK010

seem to be very sensitive. However, these indications were not expected to be found in the prepared samples.

3.3 Eddy current results (ET)

Both components *X* and *Y* of the complex eddy current signal were recorded. The lift-off signal was adjusted by means of a phase rotation that it occurs in the *X*-component (standard procedure in eddy current testing). For the representation, we only used the amplitudes of the *Y*-channel which mostly contain the hidden defect signals. In Fig. 16, the results of all defects I–IV of sample PK007

for two different testing frequencies (left: $f=200$ kHz and right: $f=500$ kHz) using probe AN 16 are shown. Due to reduced skin depth of eddy currents for higher test frequencies, the detected signal amplitudes of the defects decrease in the case of 500 kHz compared to 200 kHz.

In the case of the PK010 sample, which was measured before cutting into pieces, the results are shown in Fig. 17 again for frequencies 200 kHz and 500 kHz.

Due to the directional dependence of probe AN 16, further scans were performed using probe A 05 for PK010. In Fig. 18, the scan for test frequency 500 kHz is presented. Here, the I-shape of defect IV and I which correlates with

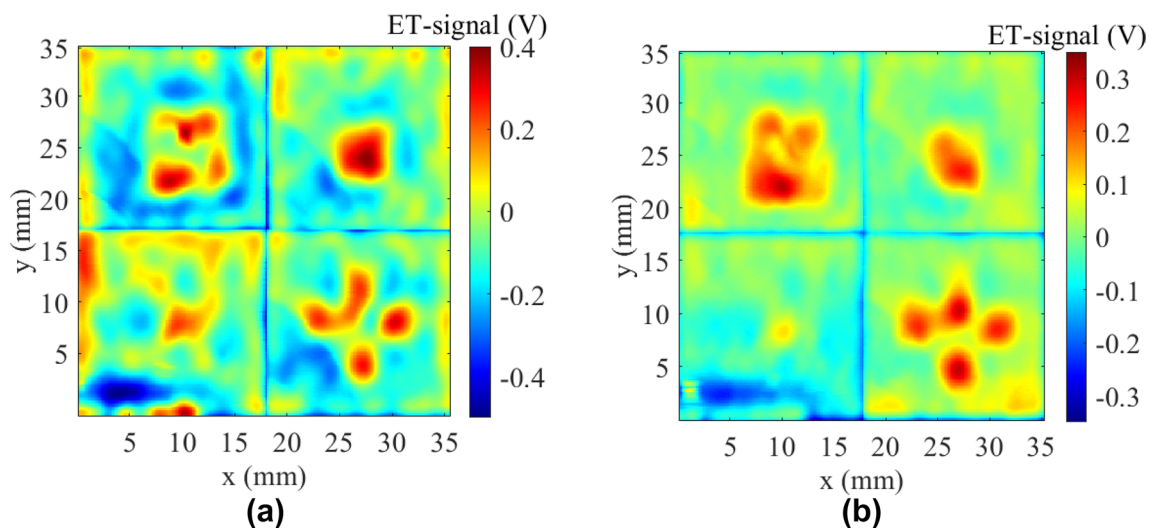


Fig. 16 Y-channel of the measured ET-signals for sample PK007. (a) Results obtained using an excitation frequency of 200 kHz. (b) Test frequency was 500 kHz

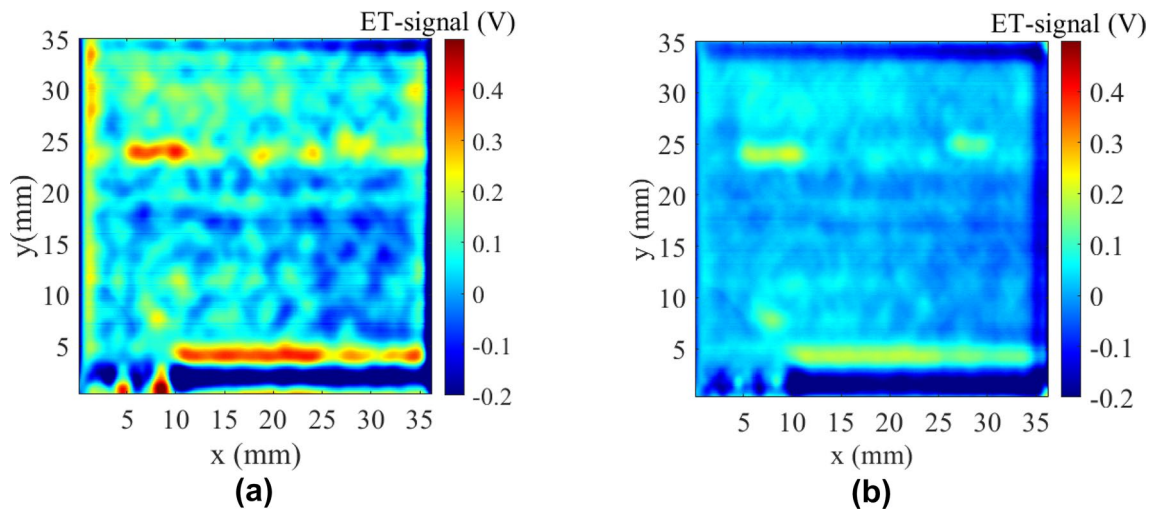


Fig. 17 Y-channel of the measured ET-signals for sample PK010 for an excitation frequency of 200 kHz (a) and a test frequency of 500 kHz (b) using probe AN 16

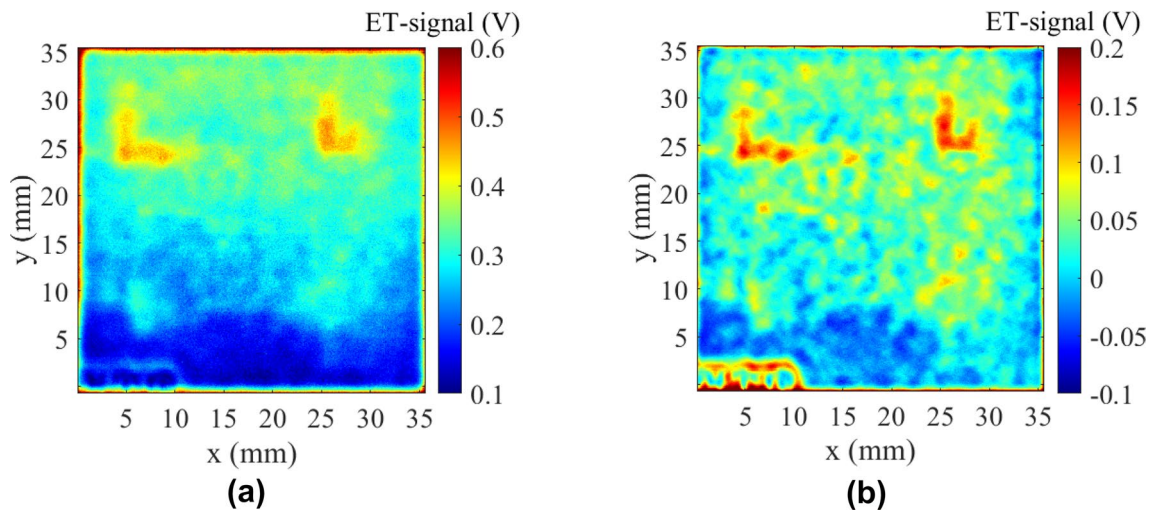


Fig. 18 Y-channel of the measured ET signals for sample PK010 for an excitation frequency of 200 kHz (a) and a test frequency of 500 kHz (b) using probe A 05

CT results is visible due to the characteristics of probe A 05.

4 Discussion

To compare the two NDT methods used in this work, only one defect for each specimen has been considered, avoiding defects with particular criticalities and pronounced edge effects (especially for thermography). In particular, for the PK007 sample, the choice fell on defect II, while for specimen PK010 on defect IV.

To compare quantitatively the two different methods TT and ET, it was necessary to refer to a normalized index capable of characterizing the defect and providing the same scale, despite the differences of the two techniques. In this case, the normalized contrast or contrast-to-noise ratio (CNR) has been chosen, defined as:

$$\text{CNR} = \frac{\text{MS}_D - \text{MS}_S}{\text{SD}_S} \quad (1)$$

where MS_D is the mean value of the defect signal, MS_S is the mean value of the sound and SD_S is the standard deviation of the sound. The area immediately around the selected defect,

Fig. 19 Comparing the obtained results for TT and ET. Zoom of the defect II—PK007, (a) TT 1.22 Hz, (b) ET probe AN 16 500 kHz. Contours of the ROEDs and identification of the chosen sound zone that is defined as all the area except the ROED

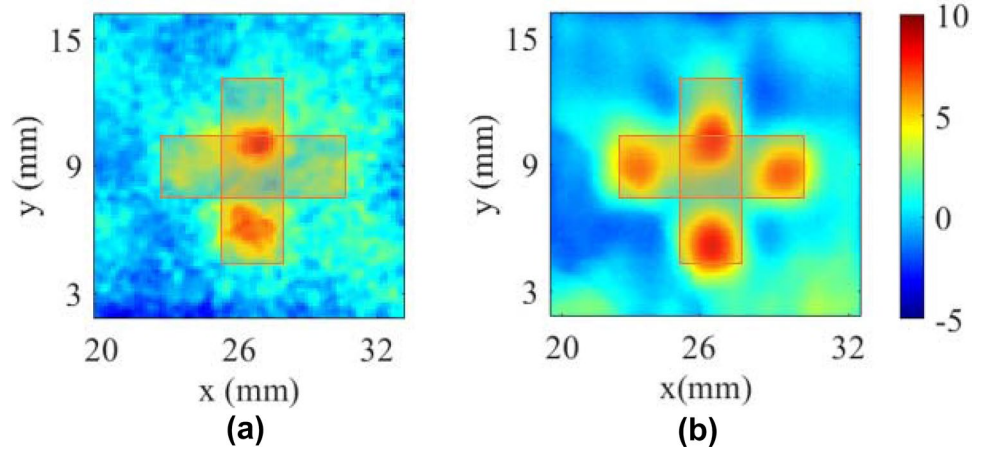
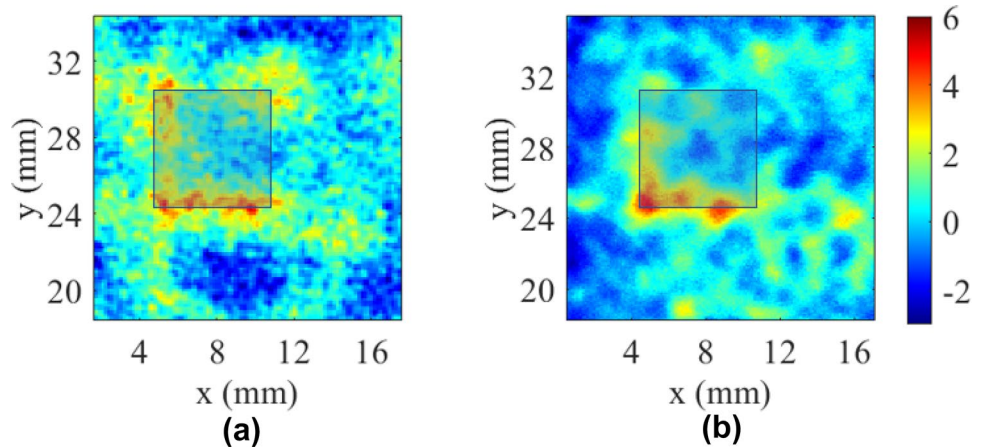


Fig. 20 Comparing the obtained results for TT and ET. Zoom of the defect IV—PK010, (a) TT 0.98 Hz, (b) ET A 05 500 kHz zoom defect IV. Contours of the ROEDs and identification of the chosen sound zone that is defined as all the area except the ROED



outside the region of expected defect (ROED—region of expected defect, Figs. 19, 20) has been considered as the sound.

4.1 PK007 (keyhole mode)

The results related to the two techniques TT and ET are reported in Fig. 19, considering the specified defects and the most significant results. The TT result corresponds to Fig. 12b and the ET result to Fig. 16b, with a zoom in correspondence of the defect II.

For completeness, the ROED is also shown in both images.

Although CNR values of the defect from TT and ET results are comparable, the ET results appear more smooth in general. This can be explained by the effective width of the used coil (in the range of the coil diameter 1.6 mm). In case of a grainy surface with typical grain sizes between 0.1 and 1 mm, this sensor acts like a low-pass filter and blurs fine details. Despite the resulting spatial resolution was high enough to indicate the four separate clusters detected by CT,

the two in the middle has a quite compact shapes, while the other two are more fissured e.g., their surface to volume ratio is higher (see Fig. 7).

In contrast, the TT could only clearly identify the two middle clusters, while the left one is barely indicated and the right one not detectable against the background. The authors can conclude that TT seems less capable for detecting these fissured structures, in comparison to ET. However, considering the phase data obtained with a higher frequency, at least the left cluster could also be detected by TT, as shown in Fig. 19a. In other words, it is necessary to investigate all the frequencies for reconstructing and characterizing volumetric defects with the PPT data [23].

4.2 PK010 (lack of fusion mode)

Regarding the sample PK010, the discussion has been focused on the defect IV in the upper left quarter, selecting for TT the frequency of 0.37 Hz (a zoom of the Fig. 13b), and for ET a part of the result already shown in Fig. 18.

For the PK010 sample, the laser power was reduced which led to regions with a lack of fusion as artificial

defects. Both methods give similar defect geometries. The horizontal lower edge is blurred in comparison to the CT results, and both methods reveal a substructure of this edge not recognizable in the CT result (see Fig. 9a). Furthermore, ET and TT results present a narrowing of or even a gap within the left vertical edge not provided by CT.

In addition to the cluster-related signals, the ET data present a characteristic signal pattern which is fluctuating across the surface of the test samples. This pattern is more visible for the PK010 than for PK007 where ET signals are smoothed. This behavior can be explained by the use of the testing coils. For the PK007 sample, the used coil diameter of probe AN16 was 16 mm and 5 mm in case of probe A05 (PK010). The reduced diameter for A05 leads to an enhanced spatial resolution and, therefore, a more blotchy signal pattern due to material's inhomogeneity. The origin of this inhomogeneity is not fully understood and basis of further investigation. At this moment, it is not clear whether the granular surface structure or currently unknown fluctuations in the material parameters are the cause for the ET background pattern.

In addition, the right choice of the applied ET set-up and which coil system should be used plays an important role. In the case of spherical defects, the probe with a directional dependency is beneficial due to its better detectability leading to enhanced CNR values. However, if the shape of

defects is non-spherical, an absolute probe with a non-directional behavior should be used.

4.3 Quantitative comparison between TT and ET

Table 5 shows the maximum CNR values for both the selected defects, referred to the results reported in Figs. 19 and 20 and considering an area of 3×3 pixels around the pixel with the highest CNR value. The CNR values confirm similar results for the two techniques, with slightly higher values for the TT in the case of keyhole defects.

To obtain the in-plane dimension of the defected area, a binarization analysis of TT and ET data, adopting a decision threshold values criterion [40] has been performed. In this way, the detectable and undetectable defects were expressed as 1 and 0 (hit/miss data). In particular, the generic pixel (x, y) with normalized contrast CNR has been identified as a defect if the inequality (Eq. 2) occurred:

$$\text{CNR}(x, y) = \frac{\text{MS}_D - \text{MS}_s}{\text{SD}_s} > \text{Th}, \quad \text{with } \text{MS}_D - \text{MS}_s > 0, \quad (2)$$

where Th is the threshold value, usually an integer between 1 and 3.

Given the differences between the two adopted techniques, the threshold values can obviously be different. As already said, for the ET data, two different probes were used for detecting defects in the samples PK007 and PK010. In view of this, and as it can be seen in Figs. 19 and 20, the ET data of the two samples are characterized by a different signal-to-noise ratio that involves a different CNR value. In this regard, two different values of Th have been chosen for binarizing the ET data of samples PK007 and PK010 (3 and 2 respectively). For TT data, the same threshold value of 2 has been used for obtaining the binary maps related to the two samples.

Table 5 Comparison in terms of maximum CNR value between TT and ET results

Specimen	Defect	TT CNR	ET CNR
PK 007 TT @ $f=1.22$ Hz ET @ $f=500$ kHz with AN 16	II	8.7	7.5
PK 010 TT @ $f=0.98$ Hz ET @ $f=500$ kHz with A 05	IV	5.1	4.7

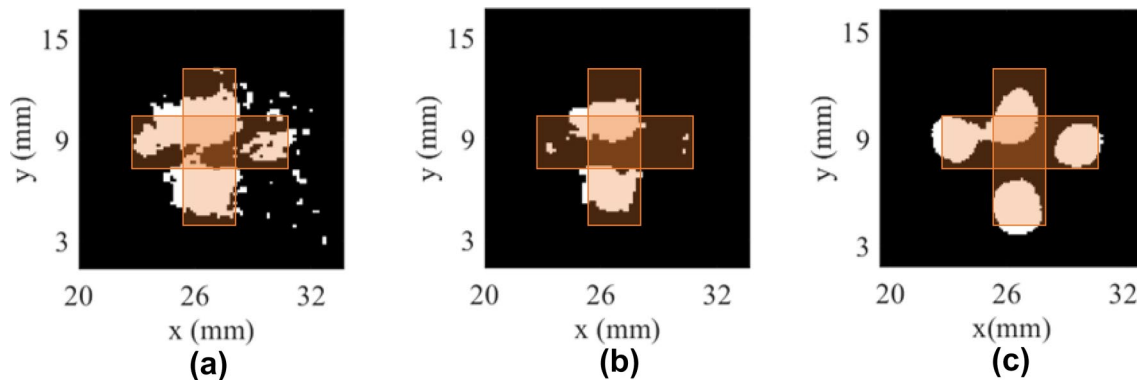


Fig. 21 Comparing the obtained results for TT and ET. Zoom of the defect II—PK007, (a) TT 1.22 Hz Th=2, (b) TT 1.22 Hz Th=3, (c) ET AN 16 500 kHz Th=3. Binarized maps

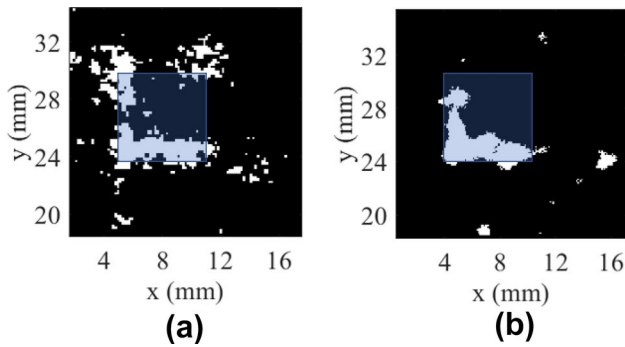


Fig. 22 Comparing the obtained results for TT and ET. Zoom of the defect IV—PK010, (a) TT 0.98 Hz, (b) ET A 05 500 kHz. Binarized maps, Th=2 for both the images

In Figs. 21 and 22, the binarized maps are reported for PK007 and PK010 and for both techniques. To show the effect of the Th value on the binary data, also the result for Th=3 is reported (Fig. 21b).

The ET results seem to reveal better the contour of the four clusters related to the cross defect with respect to the TT data in which the defect areas appear more shaded (Fig. 21).

Different results for ET comparing PK007 and PK010 are due to the use of two different probes, as already discussed in the previous section. In comparison with TT results (Th=2), ET result presents fewer false positives, with a slightly more precise contour of the defect. This is partly due to the high frequency chosen for the TT phase data characterized by a lower signal-to-noise ratio than low-frequency data. However, as already shown in the previous section, the higher frequencies phase data allow to detect and reconstruct the L-shape of the defect as detected by the μ CTs (Fig. 13a).

In the case of the sample PK007, ET seems to provide better results than TT in terms of area actually defective, if compared to the μ CT results. In particular, a slight overestimation of the defect area is obtained for both techniques, allowing to indicate the right and left clusters with the choice of the lower threshold value for TT. Referring to the TT technique, the threshold value equals to 3 (the same adopted for the ET), leads to underestimate the area of the defect, which is not a good practice for an NDT inspection.

In Table 6, a quantitative comparison between the two techniques is reported. In particular, both the in-plane defect area and the percentual of defected areas with respect to the nominal size of the ROED are depicted.

An estimation of the detection limits is possible for both techniques knowing the actual defect dimensions from the μ CT data. In case of keyhole mode defects, the detection limit can be directly assessed considering the minimum detectable cluster size. A different approach has been used for the lack of fusion defects. In this case, we focused on the cluster regions located at the edges of the imposed defects and then, the detection limit was regarded in relation to the micropore concentration provided by Fig. 8. In this way, the concentration of 0.8 micropores/mm³ seems to be sufficient to detect defect III with a width of 0.3 mm, but not to detect defect II with lower values around 0.5 micropores/mm³. Table 7 provides an overview of the estimated detections for both defect types.

It is important to underline as these limits strictly refer to the adopted set-up, instrumentation, test parameters and data processing. However, the numbers can provide the first indication about typical detection limits of the two techniques.

Table 6 A comparison in terms of 2D extent of the defect between TT and ET results

specimen	defect	CT area mm ²	(%With respect to the ROED)	TT area mm ²	% With respect to the ROED	ET area mm ²	(%With respect to the ROED)
PK 007	II	12.4	34.5%	Th \geq 2	Th \geq 2	16.82	46.7%
TT @ f=1.22 Hz				18.9	52.5%		
Th=2; Th=3				Th \geq 3	Th \geq 3		
ET @				9.2	25.6%		
f=500 kHz							
with AN 16							
Th=3							
PK 010	IV	5.9	16.4%	12.8	35.4%	11.1	30.8%
TT @ f=0.91 Hz							
Th=2							
ET @							
f=500 kHz							
with A 05							
Th=2							

Table 7 Comparison in terms of detection limits between TT and ET results

Specimens and typical defects	TT (PPT different frequencies)	ET (different probes at 500 kHz)
PK007	> 2 mm × 1 mm	< 2 mm × 1 mm
Keyhole mode defects	Not detected defect III (see Fig. 12)	Clearly detected defect III (see Fig. 16b)
PK010	> 0.5 micropores/mm ³	≥ 0.8 micropores/mm ³
Lack of fusion mode defects	Not detected defect II (see Fig. 13)	Barely detected defect III (see Fig. 17 b)

5 Conclusion

In this work, an extensive analysis involving different NDT methods was carried out to characterize some defects typical for the L-PBF additive manufacturing process. In particular, the rise of some defective areas (here defined as ROED region of expected defect) was induced by changing the process parameters, such as the speed and the laser power.

Defect characterization with μ CT reveals that the expected defect shape did not appear. Instead, only isolated conglomerates of pores are detectable with different shapes in different depths below the surface. In case of the lack of fusion areas, the pores are concentrated at certain margins of the involved regions.

These irregular-shaped defects could be found by TT and ET techniques, but with different sensitivity for the respective microstructure. Both NDT methods have shown their potential to detect hidden defects in AM components having only one-sided access. Comparing the results TT and ET, it is possible to highlight that:

- both methods detect hidden defects with a good contrast-to-noise ratio (CNR);
- the obtained detection limits are in the same order of magnitude, but ET has a higher sensitivity to strongly fissured cluster geometries. For TT with PPT analysis, it is strongly recommended to evaluate not only one frequency with the highest available CNR, but also other higher frequencies which can reveal different defect shapes as a consequence of the irregular defect shape. However, under certain assumptions, a defect shape with its associated frequency could be related to a certain depth range, but this approach is out of the scope of this contribution.
- for TT inspections, the PPT algorithm is greatly affected by edge effects and the inspection of small specimens with defects not far from the edge might be disturbed.
- for ET measurements, the comparison of both samples shows that the right decision on which coil system should be used plays an important role. In the case of keyhole defects, the probe with a directional dependency is beneficial due to its better detectability leading to enhanced CNR values. However, if the shape of defects is non-

spherical (lack of fusion), an absolute probe with a non-directional behavior should be used.

Acknowledgements The samples used for these experiments are provided within the BAM project ProMoAM thanks for cooperation of Gunther Mohr and Kai Hilgenberg. The authors would like to thank Christiane Maierhofer and the BAM for the availability of the labs and instrumentation. Thanks also goes to Dietmar Meinel, who started some of the μ CT measurements when there was restricted access to the labs for Covid situation.

Author contributions Conceptualization and methodology: ED, RK, DP and UG; writing-original draft preparation: ED, MP, AU, RK; draft review: DP and UG; μ CT experimental tests and results: AU; TT experimental tests: ED; ET experimental tests MP and RP.

Funding Open access funding provided by Politecnico di Bari within the CRUI-CARE Agreement. This research did not receive any specific grant from funding agencies in the public, commercial, or not-for-profit sectors.

Declarations

Conflict of interest On behalf of all authors, the corresponding author states that there is no conflict of interest.

Open Access This article is licensed under a Creative Commons Attribution 4.0 International License, which permits use, sharing, adaptation, distribution and reproduction in any medium or format, as long as you give appropriate credit to the original author(s) and the source, provide a link to the Creative Commons licence, and indicate if changes were made. The images or other third party material in this article are included in the article's Creative Commons licence, unless indicated otherwise in a credit line to the material. If material is not included in the article's Creative Commons licence and your intended use is not permitted by statutory regulation or exceeds the permitted use, you will need to obtain permission directly from the copyright holder. To view a copy of this licence, visit <http://creativecommons.org/licenses/by/4.0/>.

References

1. DebRoy T, Wei HL, Zuback JS, Mukherjee T, Elmer JW, Milewski JO, Zhang W (2018) Additive manufacturing of metallic components—process, structure and properties. *Prog Mater Sci* 92:112–224. <https://doi.org/10.1016/j.pmatsci.2017.10.001>
2. ASTM Committee F42 on Additive Manufacturing Technologies, & ASTM Committee F42 on Additive Manufacturing Technologies. Subcommittee F42. 91 on Terminology (2012) Standard

- terminology for additive manufacturing technologies. Astm International
3. Mani M, Feng S, Brandon L, Donmez A, Moylan S, Feserman R (2017) Measurement science needs for real-time control of additive manufacturing powder-bed fusion processes. CRC Press, Boca Raton, pp 629–652. <https://doi.org/10.1201/9781315119106-34>
 4. Gordon JV, Narra SP, Cunningham RW, Liu H, Chen H, Suter RM, Rollett AD (2020) Defect structure process maps for laser powder bed fusion additive manufacturing. *Addit Manuf* 36:101552. <https://doi.org/10.1016/j.addma.2020.101552>
 5. King WE, Barth HD, Castillo VM, Gallegos GF, Gibbs JW, Hahn DE, Rubenchik AM (2014) Observation of keyhole-mode laser melting in laser powder-bed fusion additive manufacturing. *J Mater Process Technol* 214(12):2915–2925. <https://doi.org/10.1016/j.jmatprotec.2014.06.005>
 6. Kladovasilakis N, Charalampous P, Kostavelis I et al (2021) Impact of metal additive manufacturing parameters on the powder bed fusion and direct energy deposition processes: a comprehensive review. *Prog Addit Manuf* 6:349–365. <https://doi.org/10.1007/s40964-021-00180-8>
 7. Coeck S, Bisht M, Plas J, Verbist F (2019) Prediction of lack of fusion porosity in selective laser melting based on melt pool monitoring data. *Addit Manuf* 25:347–356. <https://doi.org/10.1016/j.addma.2018.11.015>
 8. Vecchiato FL, de Winton H, Hooper PA, Wenman MR (2020) Melt pool microstructure and morphology from single exposures in laser powder bed fusion of 316L stainless steel. *Addit Manuf* 36:101401. <https://doi.org/10.1016/j.addma.2020.101401>
 9. Zikmund T, Šalplachta J, Zatočilová A, Břínek A, Pantělejev L, Štěpánek R, Kaiser J (2019) Computed tomography based procedure for reproducible porosity measurement of additive manufactured samples. *NDT E Int* 103:111–118. <https://doi.org/10.1016/j.ndteint.2019.02.008>
 10. DuPlessis A, Yadroitsev I, Yadroitsava I, LeRoux SG (2018) X-ray microcomputed tomography in additive manufacturing: a review of the current technology and applications. *Print Addit Manuf* 5(3):227–247. <https://doi.org/10.1089/3dp.2018.0060>
 11. Stern F, Tenkamp J, Walther F (2020) Non-destructive characterization of process-induced defects and their effect on the fatigue behavior of austenitic steel 316L made by laser-powder bed fusion. *Prog Addit Manuf* 5:287–294. <https://doi.org/10.1007/s40964-019-00105-6>
 12. Thanki A, Goossens L, Mertens R, Probst G, Dewulf W, Witvrouw A, Yang S (2019) Study of keyhole-porosities in selective laser melting using X-ray computed tomography. In: *Proceedings of iCT 2019*, pp 1–7. <https://doi.org/10.29007/3qvj>
 13. Ronneberg T, Davies CM, Hooper PA (2020) Revealing relationships between porosity, microstructure and mechanical properties of laser powder bed fusion 316L stainless steel through heat treatment. *Mater Des* 189:108481. <https://doi.org/10.1016/j.matdes.2020.108481>
 14. Mohr G, Altenburg SJ, Hilgenberg K (2020) Effects of inter layer time and build height on resulting properties of 316L stainless steel processed by laser powder bed fusion. *Addit Manuf* 32:101080. <https://doi.org/10.1016/j.addma.2020.101080>
 15. Altenburg SJ, Maierhofer C, Gumenyuk A (2018) Comparison of MWIR thermography and high-speed NIR thermography in a laser metal deposition (LMD) process. In: *Proceedings of conference QIRT 2018*, QIRT Council, pp 1–5. <https://doi.org/10.21611/qirt.2018.p35>
 16. Baumgartl H, Tomas J, Buettner R et al (2020) A deep learning-based model for defect detection in laser-powder bed fusion using in-situ thermographic monitoring. *Prog Addit Manuf* 5:277–285. <https://doi.org/10.1007/s40964-019-00108-3>
 17. Chen Y, Peng X, Kong L, Dong G, Remani A, Leach R (2021) Defect inspection technologies for additive manufacturing. In *J Extreme Manuf* 3(2):022002. <https://doi.org/10.1088/2631-7990/abe0d0>
 18. Davis G, Nagarajah R, Palanisamy S, Rashid RAR, Rajagopal P, Balasubramaniam K (2019) Laser ultrasonic inspection of additive manufactured components. *Int J Adv Manuf Technol* 102(5):2571–2579. <https://doi.org/10.1007/s00170-018-3046-y>
 19. Lopez A, Bacelar R, Pires I, Santos TG, Sousa JP, Quintino L (2018) Non-destructive testing application of radiography and ultrasound for wire and arc additive manufacturing. *Addit Manuf* 21:298–306. <https://doi.org/10.1016/j.addma.2018.03.020>
 20. Cerniglia D, Montinaro N (2018) Defect detection in additively manufactured components: laser ultrasound and laser thermography comparison. *Procedia Struct Integr* 8:154–162. <https://doi.org/10.1016/j.prostr.2017.12.016>
 21. Tyagi P, Goulet T, Riso C, Stephenson R, Chuenprateep N, Schlitzer J, Garcia-Moreno F (2019) Reducing the roughness of internal surface of an additive manufacturing produced 316 steel component by chempolishing and electropolishing. *Addit Manuf* 25:32–38. <https://doi.org/10.1016/j.addma.2018.11.001>
 22. D’Accardi E, Altenburg S, Maierhofer C, Palumbo D, Galietti U (2019) Detection of typical metal additive manufacturing defects by the application of thermographic techniques. In: *Multidisciplinary digital publishing institute Proceedings*, vol 27, no. 1, p 24. <https://doi.org/10.3390/proceedings2019027024>
 23. D’Accardi E, Ulbricht A, Krakenhagen R, Palumbo D, Galietti U (2021) Capability of active thermography to detect and localize pores in metal additive manufacturing materials. In: *IOP conference series: materials science and engineering*, vol 1038, no. 1, p 012018. IOP Publishing. <https://doi.org/10.1088/1757-899X/1038/1/012018>
 24. Heifetz A, Shribak D, Zhang X, Saniie J, Fisher ZL, Liu T, Cleary W (2020) Thermal tomography 3D imaging of additively manufactured metallic structures. *AIP Adv* 10(10):105318
 25. Zhang X, Saniie J, Heifetz A (2020) Detection of defects in additively manufactured stainless steel 316L with compact infrared camera and machine learning algorithms. *JOM* 72(12):4244–4253. <https://doi.org/10.1007/s11837-020-04428-6>
 26. Libby HL (1971) *Introduction to electromagnetic nondestructive test method*. Wiley-Interscience, New York, pp 258–268
 27. Repelianto AS, Kasai N (2019) The improvement of flaw detection by the configuration of uniform eddy current probes. *Sensors* 19(2):397. <https://doi.org/10.3390/s19020397>
 28. Ghoni R, Dollah M, Sulaiman A, Ibrahim FM (2014) Defect characterization based on eddy current technique: technical review. *Adv Mech Eng* 6:182496. <https://doi.org/10.1155/2014/182496>
 29. Garcia-Martin J, Gomez-Gil J, Vazquez-Sanchez E (2011) Non-destructive techniques on eddy current testing. *Sensors* 11:2525–2565. <https://doi.org/10.3390/s110302525>
 30. Allweins K, Gierelt G, Krause HJ, Kreutzbruck M (2003) Defect detection in thick aircraft samples based on HTS SQUID-magnetometry and pattern recognition. *IEEE Trans Appl Supercond* 13(2):250–253. <https://doi.org/10.1109/TASC.2003.813696>
 31. Todorov E, Boulware P, Gaah K (2018) Demonstration of array eddy current technology for real-time monitoring of laser powder bed fusion additive manufacturing process. In: *Nondestructive characterization and monitoring of advanced materials, aerospace, civil infrastructure, and transportation XII*, vol 10599, p 1059913. International Society for Optics and Photonics. <https://doi.org/10.1117/12.2297511>
 32. Ehlers H, Pelkner M, Thewes R (2020) Heterodyne eddy current testing using magnetoresistive sensors for additive manufacturing purposes. *IEEE Sens J* 20(11):5793–5800. <https://doi.org/10.1109/JSEN.2020.2973547>

33. Mook G, Hesse O, Uchanin V (2007) Deep penetrating eddy currents and probes. *Mater Test* 49:258. <https://doi.org/10.3139/120.100810>
34. Forien JB, Calta NP, DePond PJ, Guss GM, Roehling TT, Matthews MJ (2020) Detecting keyhole pore defects and monitoring process signatures during laser powder bed fusion: a correlation between in situ pyrometry and ex situ X-ray radiography. *Addit Manuf* 35:101336. <https://doi.org/10.1016/j.addma.2020.101336>
35. Mohr G, Altenburg SJ, Ulbricht A, Heinrich P, Baum D, Maierhofer C, Hilgenberg K (2020) In-situ defect detection in laser powder bed fusion by using thermography and optical tomography—comparison to computed tomography. *Metals* 10(1):103. <https://doi.org/10.3390/met10010103>
36. Ibarra-Castaneda C, Maldague XP (2004) Defect depth retrieval from pulsed phase thermographic data on plexiglas and aluminum samples. In: *Thermosense XXVI*, vol 5405, pp 348–357. International Society for Optics and Photonics. <https://doi.org/10.1117/12.540855>
37. D'Accardi E, Palano F, Tamborrino R, Palumbo D, Tatì A, Terzi R, Galietti U (2019) Pulsed phase thermography approach for the characterization of delaminations in cfrp and comparison to phased array ultrasonic testing. *J Nondestr Eval* 38(1):20. <https://doi.org/10.1007/s10921-019-0559-8>
38. Marinetti S, Plotnikov YA, Winfree WP, Braggiotti A (1999) Pulse phase thermography for defect detection and visualization. In: *Nondestructive evaluation of aging aircraft, airports, and aerospace hardware III*, vol 3586, pp 230–238. International Society for Optics and Photonics. <https://doi.org/10.1117/12.339890>
39. Maierhofer C, Röllig M, Krankenhagen R, Myrach P (2016) Comparison of quantitative defect characterization using pulse-phase and lock-in thermography. *Appl Opt* 55(34):D76–D86. <https://doi.org/10.1364/AO.55.000D76>
40. Tamborrino R, Palumbo D, Galietti U, Aversa P, Chiozzi S, Luprano VAM (2016) Assessment of the effect of defects on mechanical properties of adhesive bonded joints by using non destructive methods. *Compos B Eng* 91:337–345. <https://doi.org/10.1016/j.compositesb.2016.01.059>

Publisher's Note Springer Nature remains neutral with regard to jurisdictional claims in published maps and institutional affiliations.